Thermohydrodynamics of an evaporating droplet studied using a multiphase lattice Boltzmann method

Ahad Zarghami[1,*] and Harry E. A. Van den Akker[2,3]
[1]*Department of Process and Energy, TU Delft, Netherlands*
[2]*Transport Phenomena Group, Department of Chemical Engineering, TU Delft, Netherlands*
[3]*Bernal Institute, School of Engineering, University of Limerick, Ireland*
(Received 16 December 2016; published 27 April 2017)

In this paper, the thermohydrodynamics of an evaporating droplet is investigated by using a single-component pseudopotential lattice Boltzmann model. The phase change is applied to the model by adding source terms to the thermal lattice Boltzmann equation in such a way that the macroscopic energy equation of multiphase flows is recovered. In order to gain an exhaustive understanding of the complex hydrodynamics during evaporation, a single droplet is selected as a case study. At first, some tests for a stationary (non-)evaporating droplet are carried out to validate the method. Then the model is used to study the thermohydrodynamics of a falling evaporating droplet. The results show that the model is capable of reproducing the flow dynamics and transport phenomena of a stationary evaporating droplet quite well. Of course, a moving droplet evaporates faster than a stationary one due to the convective transport. Our study shows that our single-component model for simulating a moving evaporating droplet is limited to low Reynolds numbers.

DOI: 10.1103/PhysRevE.95.043310

I. INTRODUCTION

The phenomenon of falling droplets undergoing a phase change happens in many engineering machines, such as combustion engines [1]. Therefore an efficient and proper design of these machines requires comprehensive knowledge of a single-droplet dynamics in multiphase flow as well as detailed understanding of the influence of various physical properties on the dynamics of a droplet.

The complexity of the numerical simulation of two-phase flow with phase change is due to the deformability and the motion of the interface between the phases. The simulation of an evaporating droplet requires tracking interface motion during phase change; computing mass, momentum, and heat transfer across the interface; and hydrodynamics of the flow. Therefore the development of an effective numerical model can have a large impact on the simulation results. For this purpose, many numerical approaches were developed to model multiphase flows and interface motion [1–3].

The computational models based on the Navier-Stokes equations are divided into interface-tracking [4–6] and interface-capturing categories [7–9]. While the interface curvature is predicted accurately in interface-tracking methods, these methods need complex boundary problems and complicated dynamic meshing algorithms. These limitations are alleviated by using interface-capturing models such as volume of fluid [8], and level set methods [9]. In these methods, all phases and components of the flow are modeled as a single continuum with discontinuous properties at the interfaces and a specific scheme is defined to impose jump conditions across the interface for macroscopic properties such as density, viscosity, and pressure [8]. Overall, tracking or capturing the interface and generating a dynamic mesh are always a challenging issue, especially for rapidly transient cases, high-density ratio flows, and problems with complex geometries [10]. Moreover, the interface-tracking methods usually have great computation costs [11].

Modeling multiphase flows undergoing phase change involves accounting for the dynamics of liquid and gas phases as well as the interface. The phase separation and the formation of the interface are the consequence of molecular interactions which are neglected in traditional Navier-Stokes based multiphase models. Therefore, there is a necessity for alternative techniques to comprehend the connection between the macroscopic phenomena and the underlying molecular interactions. The lattice Boltzmann method (LBM) has received extensive attention and has become a capable simulation tool in modeling multiphase flows [11,12]. The kinetic nature and mesoscopic scale of the LBM lead to predicting the behavior of the interface dynamics and complex boundaries correctly. Various lattice Boltzmann approaches have been proposed for simulating multiphase flows including: the color-gradient LBM [13,14], the pseudopotential LBM [11,15], the free-energy LBM [16,17], the phase-field LBM [18,19], the entropic LBM [20], and the discrete Boltzmann equation [21].

Among all these methods, the pseudopotential LBM (PP-LBM) proposed by Shan and Chen [15] is a very popular model due to its straightforward algorithm. In the PP-LBM model, the interactions between phases are controlled by an interaction potential term and the phase separation occurs automatically, without resorting to any techniques to track or capture interfaces. The original PP-LBM suffers from a thermodynamic inconsistency and from large spurious velocities around the interface [22] and is limited to cases of a low density ratio [23]. For the sake of overcoming these drawbacks, various researchers tried to develop the PP-LBM for high density ratio and decrease the unphysical spurious velocities [10,19–26]. In our previous paper [27] we analyzed

*Present address: Department of Process and Energy, TU Delft, Leeghwaterstraat 39, 2628CD, Delft, Netherlands; a.zarghami-1@tudelft.nl

the effects of various lattice Boltzmann parameters and showed how to reduce the spurious velocities when simulating a stationary droplet with high density ratio and with heat transfer. Reviews of the theory and applications of the PP-LBM for simulating multiphase flows with phase change during the past two decades have been presented in Refs. [11,12].

To model thermal fluid flows by means of lattice Boltzmann modeling several energy-conserving approaches have been proposed which can be classified into three categories: multispeed approach, hybrid scheme, and double distribution function (DDF) approach. The multispeed approach [28,29] consists in extending the distribution function in order to obtain the macroscopic temperature. The main drawback of this approach is that it usually suffers from serious numerical instability and a narrow range of temperature variation. In the hybrid approach, the flow simulation is decoupled from the solution of the temperature equation. Especially, the flow is simulated by the LBM, while the energy equation is solved by conventional numerical methods, such as finite-volume [30,31] or finite-difference methods [32–34]. The use of high-order discretization schemes in hybrid schemes helps to further improve the numerical stability and accuracy of modeling [35,36].

The DDF approach [37,38,53] is based on the principle that the isothermal LBM can be directly derived by properly discretizing the continuous Boltzmann equation in temporal, spatial, and velocity spaces. Following the same procedure, an internal energy distribution function model is derived by discretizing the continuous evolution equation for the internal energy distribution, and then two independent distribution functions are obtained, one for the flow field and the other for the temperature field. This model assumes that the viscous dissipation and compression work can be neglected for incompressible fluids and the evolution of the temperature is given by the advection-diffusion equation. Hence, the temperature is considered as a passive scalar transported by the speed without changing the velocity field. This model has attracted much attention since its emergence for its excellent numerical stability and adjustability of the Prandtl number and has found applications in a variety of fields [39–41]. However, the DDF method includes complicated gradient terms if viscous heat dissipation and compression work are taken into account which may introduce some additional errors and do harm to the numerical stability [38]. Since in the present paper, viscous heat dissipation and compression work are neglected, the DDF is applied as a stable approach for solving the energy equation.

In this paper, we focus on the application of the PP-LBM on simulating a stationary and falling droplet undergoing phase change. In order to gain a detailed understanding of the complex physical phenomena occurring when simulating multiple droplets (e.g., inside a spray), it is useful and reasonable to start with a simple situation. Therefore, a single droplet is selected as a first step. The details of modeling and also the thermohydrodynamics of the fluid flow are discussed comprehensively.

The rest of paper is organized as follows: The PP-LBM for multiphase flow is presented in Sec. II. The thermal model for incorporating the phase change is described in Sec. III. Results and discussions are presented in Sec. IV and finally concluding remarks are given in Sec. V.

II. MULTIPHASE PPLBM

The general lattice Boltzmann equation with the Bhatnagar-Gross-Krook (BGK) approximation is derived as follows [42]:

$$\frac{f_i(\mathbf{x}+\mathbf{e}_i\Delta t,t+\Delta t)-f_i(\mathbf{x},t)}{\Delta t} = -\frac{1}{\tau}\left[f_i(\mathbf{x},t)-f_i^{eq}(\mathbf{x},t)\right]+\mathbf{S}_i, \quad (1)$$

where $\mathbf{x}$ is the spatial coordinate, t is time, $f_i(\mathbf{x},t)z$ is the density distribution function associated with discrete velocity direction i, τ is the relaxation time, and $\mathbf{S}_i$ represents a general source term added into the standard lattice Boltzmann equation. The discrete velocities $\mathbf{e}_i$ in the ith direction, for the D2Q9 lattice are given by $\mathbf{e}_0 = 0$ and $\mathbf{e}_i = \lambda_i(\cos\theta_i, \sin\theta_i)$ with $\lambda_i = 1, \theta_i = (i-1)\pi/2$ for $i = 1 \sim 4$ and $\lambda_i = \sqrt{2}, \theta_i = (i-5)\pi/2 + \pi/4$ for $i = 5-8$. The order number $i = 1-4$ and $i = 5-8$ represent the rectangular and the diagonal directions of the lattice, respectively. Also, f_i^{eq} is the equilibrium distribution function and is calculated as

$$f_i^{eq} = w_i\rho\left[1+\frac{(\mathbf{e}_i\cdot\mathbf{u}^{eq})}{c_s^2}+\frac{(\mathbf{e}_i\cdot\mathbf{u}^{eq})^2}{2c_s^4}-\frac{(\mathbf{u}^{eq}\cdot\mathbf{u}^{eq})}{2c_s^2}\right], \quad (2)$$

where $c_s = 1/\sqrt{3}$ is the lattice speed of sound; w_i are the weighting factors, equal to 4/9 for $i = 0$, 1/9 for $i = 1 \sim 4$, and 1/36 for $i = 5 \sim 8$; and $\mathbf{u}^{eq}$ is the equilibrium velocity. The local mass density, the local velocity, and the viscosity in the lattice units are calculated as $\rho = \sum_i f_i$, $\mathbf{u} = (\sum_i \mathbf{e}_i f_i)/\rho$, and $\nu = (\tau - 0.5)/3$, respectively.

In order to calculate the source term in Eq. (1), the exact difference method (EDM) is used [25]. The EDM is directly derived from the Boltzmann equation and has a great effect on numerical stability and accuracy of the solution [27,43,44]. In this scheme, the force term, the equilibrium velocity $\mathbf{u}^{eq}$, and the real fluid velocity $\mathbf{U}$ are calculated by

$$\mathbf{S}_i = f_i^{eq}(\rho,\mathbf{u}+\mathbf{F}\Delta t/\rho) - f_i^{eq}(\rho,\mathbf{u}), \quad (3)$$

$$\mathbf{U} = \mathbf{u}^{eq} = \mathbf{u} + \frac{\Delta t}{2\rho}\mathbf{F}, \quad (4)$$

where $\mathbf{F}$ is the net force including external body forces (e.g., gravity) and the mean field interparticle interaction forces; i.e., $\mathbf{F} = \mathbf{F}_{body} + \mathbf{F}_{int}$.

In the original PP-LBM [15], the interaction force for a single-component multiphase system is given by

$$\mathbf{F}_{int} = -\psi(\mathbf{x},t)G\sum_i w_i\psi(\mathbf{x}+\mathbf{e}_i\Delta t,t)\mathbf{e}_i\Delta t, \quad (5)$$

where $\Delta t = 1$ is the time interval and G denotes the interaction parameter, with $G < 0$ representing an attractive force and $G > 0$ representing a repulsive force between particles. Also, $\psi(\mathbf{x},t)$ is called the effective mass or the pseudopotential function which is a function of local density and describes the fluid-fluid interactions triggered by inhomogeneities of the density profile. To obtain a desired equation of state, the pseudopotential $\psi(\mathbf{x},t)$ is calculated by [24]

$$\psi(\mathbf{x},t) = \sqrt{\frac{2\left(p_{\mathrm{EOS}}-\rho c_s^2\right)}{G}}, \quad (6)$$

where p_{EOS} is the desired equation of state (EOS). Note that for the single-component multiphase simulations, the value of G becomes unimportant and is canceled out of the computations. The only requirement for G is to ensure that the whole term inside the square root is positive. In this paper, the Carnahan-Starling (CS) EOS is implemented as [24]

$$p_{\mathrm{EOS}} = \rho RT \frac{1+\rho+\rho^2-\rho^3}{(1-\rho)^3} - \rho^2, \tag{7}$$

where $R = 1$ is the gas constant. The reduced temperature and the reduced density are defined as $T_r = T/T_{cr}$ and $\rho_r = \rho/\rho_{cr}$, respectively, where the critical temperature and the critical density for the Carnahan-Starling EOS are equal to $T_{cr} = 0.09432$ and $\rho_{cr} = 0.11911$, respectively.

To improve the accuracy of a single-component multiphase model, we use the following expression, the so-called β scheme, for interparticle interaction force [45,46]:

$$\mathbf{F}_{ext} = -\beta\left[\psi(\mathbf{x},t)G\sum_i w_i\psi(\mathbf{x}+\mathbf{e}_i\Delta t,t)\mathbf{e}_i\Delta t\right] - \frac{1-\beta}{2}\left\{G\sum_i w_i[\psi(\mathbf{x}+\mathbf{e}_i\Delta t,t)]^2\mathbf{e}_i\Delta t\right\}, \tag{8}$$

where β is the weighting factor. By choosing a proper value for β, the thermodynamic inconsistency and magnitude of spurious currents reduce greatly [11,27]. For $\beta = 1$, the expression coincides with Eq. (5).

Considering the above-discussed procedure, the recovered macroscopic Navier-Stokes equations from the LBM are as follows:

$$\frac{\partial\rho}{\partial t} + \nabla(\rho\mathbf{U}) = -\frac{\Delta t}{2}\nabla\cdot\mathbf{F}, \tag{9}$$

$$\frac{\partial}{\partial t}(\rho\mathbf{U}) + \nabla\cdot(\rho\mathbf{U}\mathbf{U}) = -\nabla p + \nu\nabla\cdot[\rho(\nabla\mathbf{U}+(\nabla\mathbf{U})^T)] + \mathbf{F} - \frac{\Delta t}{2}\varepsilon\frac{\partial\mathbf{F}}{\partial t_1} - \Delta t\nabla\cdot\left[\frac{1}{2}(\mathbf{U}\mathbf{F}+\mathbf{F}\mathbf{U}) + \Delta t\frac{\tau}{\rho}\mathbf{F}\mathbf{F}\right]. \tag{10}$$

One can see that the additional nonlinear term is recovered from the EDM scheme. The scheme will be consistent with the macroscopic equations if the temporal and spatial changes of the force vary slightly (or the force term be constant), and the last term in brackets of Eq. (10) be negligible. However, the last term may have a great influence on the solution due to the velocity gradient. Huang *et al.* [43] showed that the term $\rho^{-1}\mathbf{F}\mathbf{F}$ is capable of enhancing numerical stability.

There are different ways of incorporating the gravitational and buoyant effects as driving force to the system:

$$\mathbf{F}_{body} = \rho\mathbf{g}, \tag{11a}$$

$$\mathbf{F}_{body} = (\rho-\rho_{vap})\mathbf{g}, \tag{11b}$$

$$\mathbf{F}_{body} = (\rho-\hat{\rho})\mathbf{g}, \tag{11c}$$

where $\mathbf{g}$ is the downward gravitational acceleration, ρ is the local density (either liquid or vapor), and $\hat{\rho}$ is the averaged density over the whole computational domain. Which of these expressions predicts the true multiphase behavior best, depends on the particular problems simulated. For the simulation of a falling droplet in a periodic domain, we should adopt Eq. (11c), otherwise, the droplet will drag the liquid along with itself and the multiphase system will continue to accelerate downwards, as there is no solid wall which can provide the friction drag force to balance the gravitational force. By using Eq. (11c), we ensure that the average value of $\mathbf{F}_{body}$ in the periodic domain is zero and no net momentum is added to the system so that the mass-average velocity of the mixture in the computational domain remains independent of time [47]. In all our simulations of a falling droplet, the initial mass-average velocity of the mixture in the periodic domain was zero. However, as the droplet fell, the surrounding vapor acquired a small upward velocity.

III. THERMAL MODEL

Ignoring viscous heat dissipation, the thermal LBM based on the double distribution function (DDF) model is expressed as follows [48,49]:

$$\frac{g_i(\mathbf{x}+\mathbf{e}_i\Delta t,t+\Delta t)-g_i(\mathbf{x},t)}{\Delta t} = -\frac{1}{\tau_g}\left(g_i-g_i^{eq}\right)+w_i\Lambda, \tag{12}$$

where the g_i's denote the energy distribution functions, τ_g is the thermal relaxation time, and g^{eq} denotes the energy equilibrium distribution functions given by

$$g_i^{eq} = w_i T[1+3\mathbf{e}_i\cdot\mathbf{U}]. \tag{13}$$

Also, Λ is the external source term which is added to the thermal lattice Boltzmann equation and $T = \sum_i g_i$ is the temperature. By using the Chapman-Enskog expansion one can show that the equivalent macroscopic energy equation is given in the form of

$$\frac{\partial T}{\partial t} + \nabla\cdot(\mathbf{U}T) = \nabla\cdot(\alpha\nabla T) + \Phi + \Lambda, \tag{14}$$

where $\alpha = k/\rho c_p$ is the thermal diffusivity, c_p is the specific heat at constant pressure, and k is the thermal conductivity. Also, Φ is an additional unwanted term which is introduced into the macroscopic temperature equation as the effect of the force term [50]. However, the governing energy equation for the multiphase flows with phase change in macroscopic scale is expressed as [51,52]

$$\frac{\partial T}{\partial t} + \mathbf{U}\cdot\nabla T = \frac{\nabla\cdot k\nabla T}{\rho c_p} + \Theta. \tag{15}$$

where Θ is the responsible term for the phase change and is defined as [53]

$$\Theta = \frac{1}{c_p}\left[h^{lv}\phi'(\rho)\frac{d\rho}{dt} + \frac{\dot{Q}}{\rho}\right], \tag{16}$$

where h^{lv} is the latent heat of vaporization, $\dot{Q}$ is the external heat input (per unit volume), the prime superscript denotes the derivative, and $\phi(\rho)$ is a density-dependent marker function defined such that it assumes a value of zero in the bulk vapor, unity in the bulk liquid, and increases monotonically with density in between and is defined as

$$\phi(\rho) = (\rho-\rho_{vap})/(\rho_{liq}-\rho_{vap}). \tag{17}$$

By comparing Eq. (14) with Eq. (15) one can see that Eq. (14) contains some unwanted terms and should be corrected to mimic the macroscopic energy equation, i.e., Eq. (15). Therefore, the energy source term in Eq. (12) is defined as

$$\Lambda = \underbrace{-\nabla\cdot(\alpha\nabla T) + \frac{\nabla\cdot(k\nabla T)}{\rho c_p} - \Phi + T\cdot\nabla\mathbf{U}}_{correction\ terms} + \Theta. \quad (18)$$

The extra unwanted term due to the force term is presented as [50]

$$\Phi = \left(\frac{1}{2\tau_g} - 1\right) w_i c_v T \frac{\mathbf{e}\cdot\mathbf{F}}{c_s^2}, \quad (19)$$

where c_v is specific heat at constant volume. Note that the above term does not affect the calculation of the macroscopic internal energy as its summation over i is zero. In most cases, the effect of the force term on the simulation results is negligible; however, the numerical error may be important if the correction term is comparable to the heat flux term, i.e., $k\nabla T$ [50].

By considering the correction terms and through the Chapman-Enskog expansion, the equivalent macroscopic energy equation in our simulations is expressed as

$$\frac{\partial T}{\partial t} + \mathbf{U}\cdot\nabla T = \frac{\nabla\cdot k\nabla T}{\rho c_p} + \frac{1}{c_p}\left[h^{lv}\phi'(\rho)\frac{d\rho}{dt} + \frac{\dot{Q}}{\rho}\right]. \quad (20)$$

It is worth mentioning that in order to compute $d\rho/dt$ in above equation we have to keep track of the density field at the last time step, which increases the computational cost. This issue is resolved by considering the mass conservation equation as

$$\frac{d\rho}{dt} = -\nabla\cdot(\rho\mathbf{U}). \quad (21)$$

In all simulations, the thermal diffusivities and the specific heats of the liquid and the vapor are set as $\alpha_{liq} = 10^{-3}$,$\alpha_{vap} = 10^{-2}$,$c_{p,liq} = 5.1$, and $c_{p,vap} = 2.50$, unless stated otherwise. The liquid-vapor interface properties η (such as thermal diffusivity and viscosity) are calculated by

$$\eta = [1-\phi(\rho)]\eta_{vap} + \phi(\rho)\eta_{liq}. \quad (22)$$

By using this definition, the properties change monotonically within the interface region.

IV. RESULTS

In this section, at first, the model is validated by simulating a stationary nonevaporating droplet. Then the simulation results for an evaporating droplet are presented.

A. Nonevaporating droplet

In this section, a stationary nonevaporating droplet located in the center of a fully periodic domain with mesh size 150×150 is simulated. The numerical results are obtained by equilibrating a droplet with initial diameter $D_0 = 60$ for different reduced temperatures (or density ratios). Figure 1(a) shows a comparison between the analytical coexistence curves for the CS EOS and numerical data calculated by the proposed method with $\beta = 1.25$. It is clear that the numerical results have good agreement with the theoretical data for a wide range of reduced temperatures (or density ratios). Figure 1(b) displays the density distribution versus the lattice domain at $T_r = 0.8$ and 0.6 where the density ratios ($\rho^* = \rho_{liq}/\rho_{vap}$) at $T_r = 0.8$ and 0.6 are 13.7 and 130.93, respectively.

One of the drawbacks of the original PPLBM is large spurious velocities that are formed around the curved interface. The spurious velocities have different sources, but the main source is a result of finite symmetry in the discrete velocity set and the collision and streaming dynamics. The lack of symmetry can create a slight imbalance between stresses in the interfacial regions which can cause spurious velocities [11,12]. Consequently, the magnitude of spurious velocities will increase by increasing the density ratio. Therefore by increasing the density ratio, these spurious velocities can be strong enough to dominate the solution and cause serious problems such as numerical instability or inaccuracy in the simulation. Based on the detected sources of spurious velocities there have been some suggestions regarding how to reduce their amplitude for simulation of a multiphase system

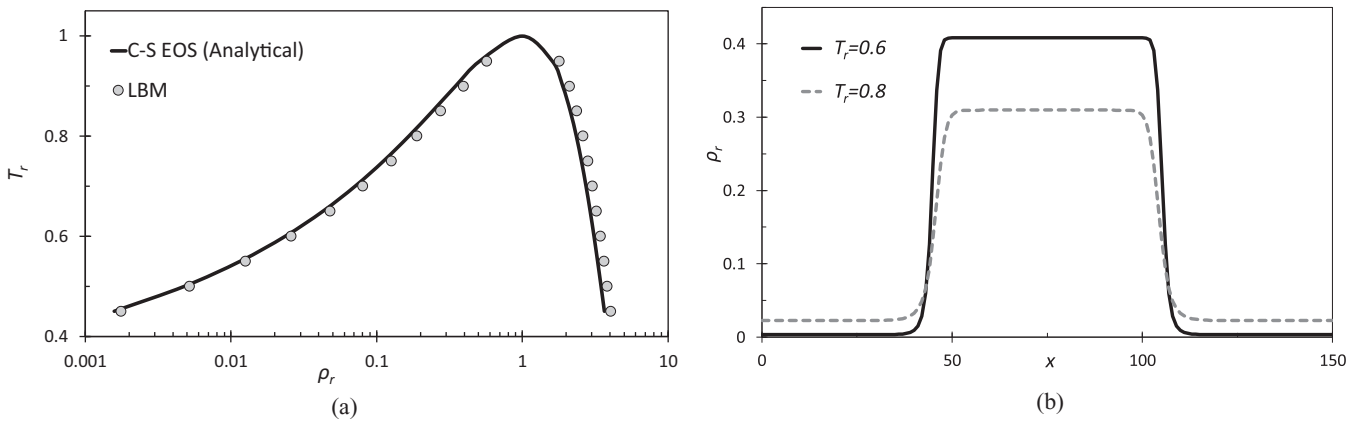

FIG. 1. (a) Liquid and vapor density variations with temperature for CS EOS; solid line: analytical solution obtained from Maxwell rule of equal areas; markers: LB simulation results by using the β-scheme force term and the EDM force implementation method; (b) equilibrium density distribution over the domain in $T_r = 0.8$ and 0.6.

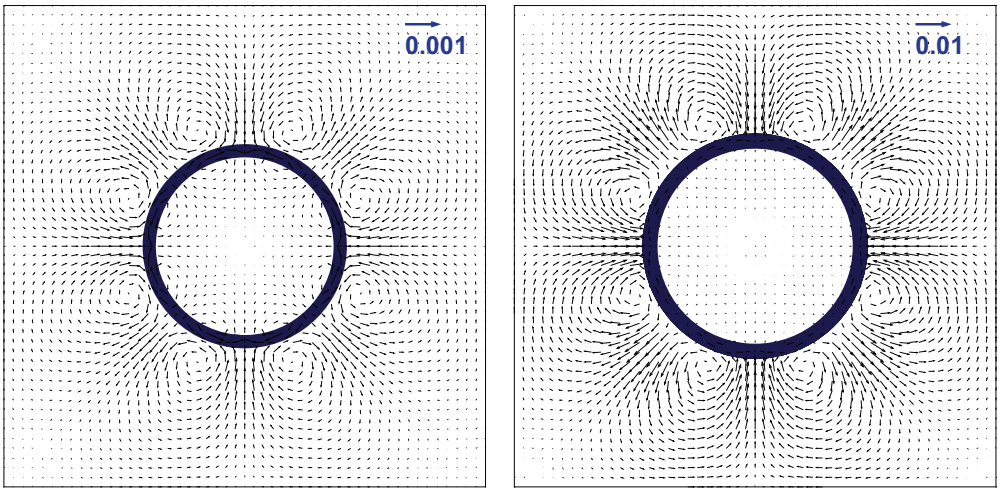

(a) (b)

FIG. 2. Spurious velocities at the gas-liquid interface at (a) $T_r = 0.8$ and (b) $T_r = 0.6$.

with curved boundary. The spurious velocities at $T_r = 0.8$ and 0.6 are shown in Fig. 2. It is clear that the spurious velocities primarily locate in the low-density (vapor) region with the maximum value around the interface region. As indicated in this figure, the maximum value of spurious velocities for $T_r = 0.8$ and 0.6 are 6×10^{-4} and 6.1×10^{-3}, respectively. By decreasing the temperature (or increasing the density ratio), the magnitude of spurious velocities increases which indicates the deviation from the real physical situation. It has been shown that due to the existence of the spurious velocities, four unphysical symmetric hot and cold spots are formed around the interface when simulating a (non-)isothermal droplet [27].

However, compared to other diffusive-interface methods, the PP-LBM usually shows smaller spurious velocities. A comparison between the PP-LBM and FV-VOF techniques (using OPENFOAM and FLUENT) is shown in Fig. 3 for $\rho^* = 15$. Note that in order to have a fair comparison, a spurious Reynolds number is calculated as ($\mathrm{Re}_{spu} = |U_{\max}| D_0/\nu$, where $|U_{\max}|$ is the maximum magnitude of the spurious velocities), so that a dimensionless comparison can be performed between

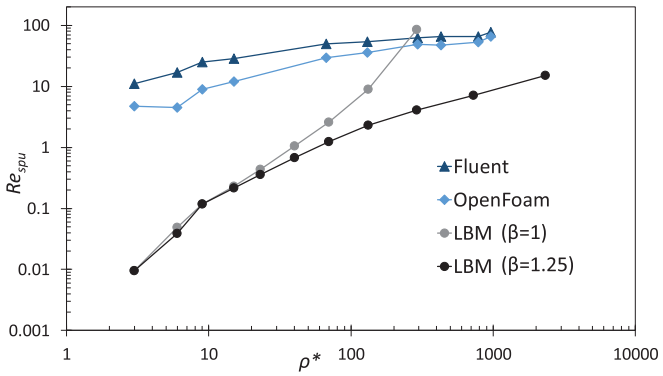

FIG. 3. Comparison of the spurious Reynolds number Re_{spu} as function of density ratio obtained from the LBM (with $\beta = 1, 1.25$) and FV-VOF implementation scheme using OPENFOAM and FLUENT solvers [56].

FVVOF and LBM, as the former works with physical units and the latter in dimensionless phase space.

The interface representation is an important aspect in two-phase flow simulations. The real physical interface thickness is very sharp and is usually several orders of magnitude smaller than the reference length scale of the problem under consideration. One important feature of the PP-LB model as a diffusive-interface model is its ability to automatically adjust the interface between the phases and computing the interface curvature. However, in this method, the sharp physical interface between phases is replaced by a thick layer in which the phases are mixed monotonically. In the PP-LBM, the interface thickness is usually quite thick and dependent upon the density ratio as it goes from 11 to 4 cells in lattice units for $\rho^* = 3$ (i.e., $T_r = 0.95$) to 9500 (i.e., $T_r = 0.4$).

Although a thick interface helps the LB model to maintain numerical stability, the accuracy is also sacrificed [54]. Generally, a sharp interface thickness is crucial for a numerical method of the diffuse type to obtain complex interfacial structures; otherwise, thick interfaces will smear them [55]. A comparison among interface thicknesses calculated by the proposed LBM and FV-VOF implementations presented in Ref. [56] shows that the interface in the LBM is thicker compared to the FV-VOF solvers.

The thick interface restricts the ability of the LBM in capturing interfacial structures equal to or less than the interface thickness. In these cases, nonphysical shrinkage arises in, e.g., the simulation of bubble or drop dynamics [57]. Therefore the LB model with thick interface thickness may need many more grid points (or even fails) to study multiphase flows with complex topology changes.

In order to check the accuracy of the scheme, the Laplace tests for droplets of various sizes at $T_r = 0.8$ and 0.6 are done. The surface tension σ of a droplet is related to the pressure difference according to the Laplace law as $\Delta p = p_{liq} - p_{vap} = \sigma/R_0$, where Δp is the difference between inner and outer pressure in a droplet of radius R_0. Figure 4(a) shows the predicted pressure differences are plotted versus the inverse of the radius. Due to the diffusive interface in the SC model,

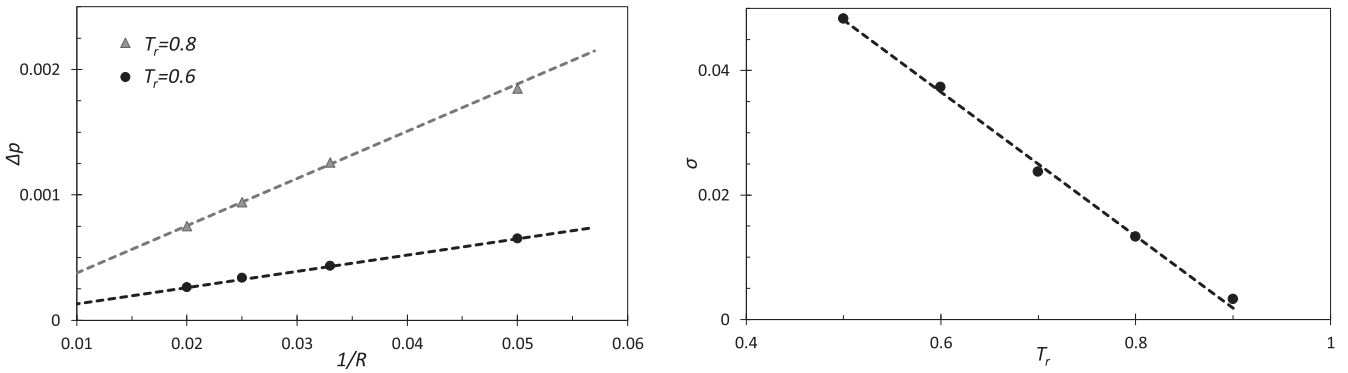

FIG. 4. (a) Verification of numerical pressure difference for $T_r = 0.8$ and 0.6 with the Laplace law (dashed lines) and (b) surface tension versus temperature.

the radius R is approximate at the position where the density is equal to $0.5\,(\rho_{liq} + \rho_{vap})$. According to the Laplace law, the plot of the pressure difference between the inside and outside of the droplet over $1/R$ should be a straight line and the slope of the plot represents the surface tension. It can be seen that the numerical results are consistent with those of the Laplace law. The surface tension comes out to be 26.4×10^{-3} and 74.6×10^{-3} for $T_r = 0.8$ and 0.6, respectively. It can be seen from Fig. 4(b) that by decreasing the temperature (or increasing the density ratio), the surface tension increases, linearly.

B. Stationary evaporating droplet

In this section, the simulation results for evaporation of a stationary droplet in a fully periodic domain are presented. After achieving the equilibrium condition for the isothermal system (at $T_r = 0.8$), the droplet is subjected to the heat flux and the latent heat of vaporization as $\dot{Q} = 1.1 \times 10^{-7}$ and $h^{lv} = 0.1$, respectively. The snapshots of the droplet at different times during the evaporation are shown in Fig. 5. Here, the dimensionless time is defined as $t = \hat{t}\alpha_{liq}/R_0^2$, where R_0 is the initial radius of the droplet and $\hat{t}$ is time in lattice units (i.e., number of iterations). These snapshots reveal that by heating up the droplet, evaporation occurs and the diameter of the droplet becomes smaller over time. It is clear that the droplet shape remains circular during the evaporation process which is consistent with theory [57].

The velocity vectors around the droplet are also shown in Fig. 5 for different times. The radial direction of the velocity vectors normal to the interface and rotational symmetry with respect to the center of the droplet are consistently reproduced as expected. As heat is absorbed by the droplet, some of the liquid particles move into the interface and then diffuse away from the droplet. Consequently, the ambient vapor also moves away from the droplet at some mean velocity that is dependent on the evaporation rate and also droplet size. The resulting flow which exists near the interface of an evaporating body and directed away from the surface is called Stefan flow. The maximum values of the velocity vectors are also shown in Fig. 5; they are 5.3×10^{-4}, 5.2×10^{-4}, and 4.4×10^{-4} at $t = 0.089$, 0.133, and 0.177, respectively. The slight decrease in velocity vectors at the last time steps is expected, as the amount of the evaporating liquid decreases and also the ambient pressure increases. It can be seen that the predicted velocity vectors are not quite radial very close to the interface

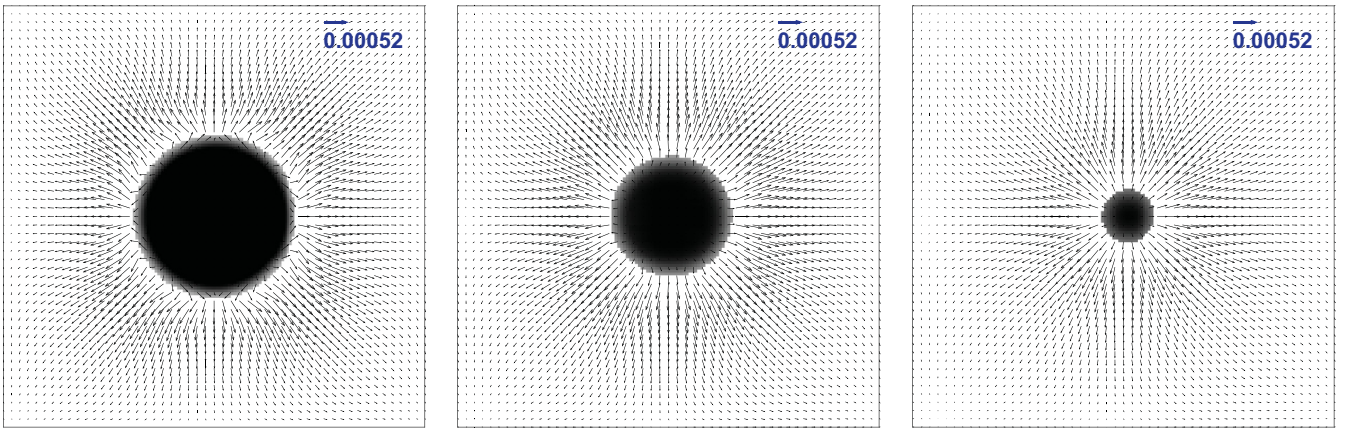

FIG. 5. The snapshots and velocity vectors of an evaporating droplet at different times: (a) $t = 0.089$, (b) $t = 0.133$, and (c) $t = 0.177$.

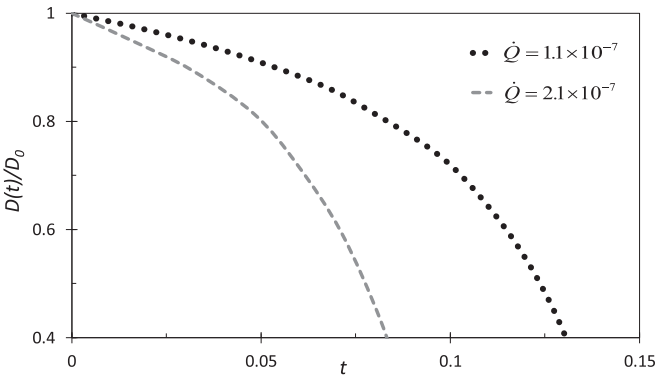

FIG. 6. Normalized droplet diameter as a function of time for different heat flux rates.

at the initial times (e.g., $t = 0.089$). This happens due to the effect of the spurious velocities on the simulation results which are almost on the same order of magnitude as the Stefan flows.

Note that the velocity vectors shown in Fig. 5 are contaminated with the spurious velocities that are local velocities in the computational domain and do not represent the true Stefan flow velocity. In order to determine the Stefan flow velocity, we consider a short time interval and calculate the shrinkage of the droplet during that interval. Then by using the following relation the correct value of the Stefan flow velocity is obtained:

$$U_{Stefan} \times \rho_{vap} = \frac{\Delta D}{\Delta t}\rho_{liq}, \tag{23}$$

where Δt and ΔD represent the time interval (here: $t = 0.0011$, or 1000 iterations in lattice units) and shrinkage of the droplet diameter, respectively. The density of vapor and liquid are constant during the short time interval. The values of the Stefan flow velocity at time $t = 0.089, 0.133$, and 0.177 are $U_{Stefan} = 8.7 \times 10^{-4}$, 17.9×10^{-4}, and 41.5×10^{-4}, respectively. By comparing U_{Stefan} with the maximum value of velocity in the computational domain, we see that U_{Stefan} is of the same order of magnitude as the local velocity at earlier times. However, the magnitude of U_{Stefan} increases with time and, consequently, the effect of the spurious velocities diminishes. These results demonstrate that the Stefan flow velocity increases with time, which is due to the faster evaporation of the droplet.

The time-dependent normalized diameter of the droplet for two uniform heat flux rates is shown in Fig. 6. By increasing the flux rate, the heat diffusion increases which results in faster evaporation. Also, it can be seen that the vaporization rate becomes faster as the droplet diameter decreases. Since the amount of transferred heat to the droplet is constant, faster evaporation is induced for the droplet with the smaller size.

The density profiles and the temperature profiles along the vertical centerline of the domain at different times are shown in Figs. 7(a) and 7(b), respectively. It clear that the density of liquid decreases during the evaporation and, proportionately, the vapor density increases with time. This phenomenon happens when a fully periodic boundary condition is set for the fluid flow. According to results of Fig. 7(a) it can be understood that the pressure changes during the evaporation and, consequently, in addition to the heating up the droplet, the change in pressure has a role in evaporation. In fact, the ambient (vapor) pressure increases with time which may result in a decrease in evaporation rate. Therefore, in order to eliminate this unwanted effect and validate the model we have to take into account some simplifications and change the boundary conditions. Further discussions will be reported in the last paragraphs of the current section.

The temperature profiles in Fig. 7(b) show that by starting the droplet heating, the temperature in the droplet increases. Due to the evaporation, a part of this heat is transferred by the evaporated liquid particles to the ambient vapor which results in an increase of the ambient (vapor) temperature. The temperature of the vapor is less than the liquid in the first time steps (i.e., $t < 0.01$); however, as more and more vaporization occurs, the amount of heat supplied to the vapor increases and a nearly parabolic profile is formed for the vapor phase. The vapor heats up faster and its temperature becomes higher than the liquid as its density (thermal diffusivity) is less (higher) than that of the liquid. The nearly flat temperature of the liquid phase can be traced to its higher thermal conductivity. Similar to density profiles, as more and more vaporization occurs the temperatures of the phases approach each other. The droplet is vaporized completely at $T_r < 1$.

It can be seen from Fig. 7(b) that the temperature in the vapor region is higher than that of the droplet. Therefore,

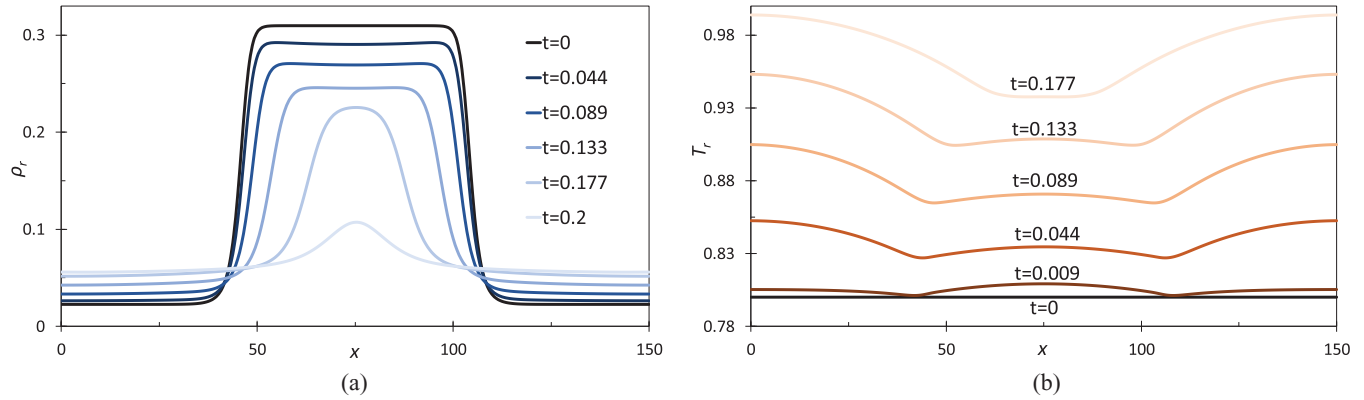

FIG. 7. (a) Density and (b) temperature profiles at different times for a droplet exposed to uniform heating which causes the vaporization.

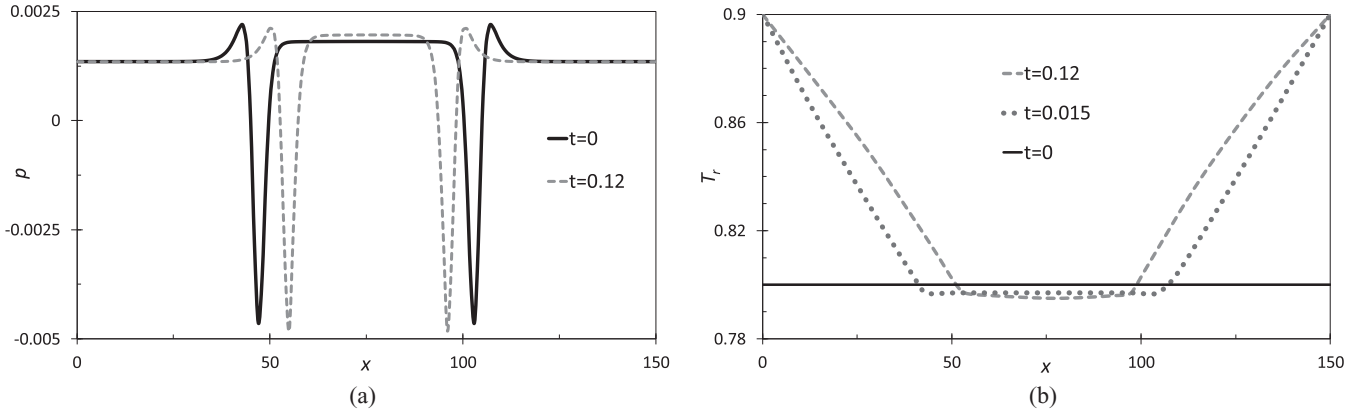

FIG. 8. (a) Pressure and (b) temperature distribution along the symmetric line of the domain at different times when using constant pressure boundary condition.

a temperature gradient exists between the droplet and the surrounding vapor resulting in conductive heat transfer from the vapor to the droplet. The conductive heat transfer is expressed by Fourier's law as $\vec{q}_{cond} = -k\nabla T$, where k is the vapor thermal conductivity and ∇T is the temperature gradient. On the other hand, a convective flow exists in the domain resulting in the transfer of heat from the droplet to the surrounding vapor by the Stefan flow as $\vec{q}_{conv} = \rho c_p T U_{Stefan}$. The maximum value of conduction heat transfer at time $t = 0.089, 0.133$, and 0.177 is $\vec{q}_{cond} = 1.2 \times 10^{-6}, 1.7 \times 10^{-6}$, and 1.9×10^{-6}, respectively. The values of the convection heat transfer at the same time are calculated as $\vec{q}_{conv} = 5.9 \times 10^{-5}, 1.6 \times 10^{-4}$, and 4.6×10^{-4}, respectively. It is clear that the order of magnitude of the convective heat transfer is higher than the conductive heat transfer. Thus convection from the droplet to the vapor is the dominant heat transfer mechanism during the evaporation.

It is necessary to validate the dynamics of phase change using the proposed method. An analytical solution for the droplet evaporation only due to the diffusion is given by the so-called D^2 law. In this analytical solution, the temperature of the droplet and the ambient (vapor) pressure should be constant during the evaporation. As we discussed earlier, the pressure does not remain constant during the evaporation of a droplet in a fully periodic domain. In order to keep the vapor pressure constant, a constant pressure boundary condition is implemented [58]. Also, the droplet heating should be eliminated; i.e., $\dot{Q} = 0$. After achieving the equilibrium condition for the isothermal system (at $T_r = 0.8$), the temperature at the boundaries is set to $T_r = 0.9$. The vapor is heated up due to this temperature rise at the boundaries and, consequently, the evaporation only due to the diffusion happens.

To keep the pressure constant, at first, the Neumann boundary condition is applied to the velocity to approximate the unknown indices f_i at the boundaries. Then, a new equilibrium distribution function, $f_i^{eq,new}$ is calculated for the local lattices with the desired density to be fixed (based on the initial pressure and current temperature) [58]. Finally, the unknown distribution functions are calculated as $f_i^{unknown} = f_i + f_i^{eq,new} - f_i^{eq}$, where f_i^{eq} is the equilibrium function with the actual density.

Figure 8 shows the pressure and temperature distributions during the evaporation when the above-described boundary condition is adopted. It is clear from Fig. 8(a) that the pressure in the bulk regions remains constant during the evaporation. However, there are variations of the pressure across the interface, which indicates that the mechanical stability condition is not satisfied around the interface. This issue happens in the lattice Boltzmann methods by using a force to introduce the nonideal EOS (for more details see [59–62]). The temperature distributions at different times are also shown in Fig. 8(b). It can be seen that the temperature in the droplet remains constant while evaporating.

The D^2 law which is also termed the quasisteady model, states that during the vaporization process, the droplet surface area, represented by the droplet-squared diameter, decreases with its lifetime as [62]

$$D^2\left[0.5 + \ln\frac{L}{D}\right] = D_0^2\left[0.5 + \ln\frac{L}{D_0}\right] - \frac{8\alpha_i \rho_i t}{\rho_{liq}} \ln(1+B), \tag{24}$$

where L is the length of the domain, D is the instantaneous diameter, and the subscript i refers to quantities evaluated at the interface. Also, $B = c_p(T_{wall} - T_i)/h^{lv}$ is the nondimensional Spalding number. Figures 9(a) and 9(b) present the time histories of the normalized squared diameter of the droplet for various temperatures of the domain boundaries and different latent heat values, respectively. The numerical results are compared with the solution of the D^2 law, and good agreements are observed. However, the deviations from the D^2 law are observed as the droplet shrinks more for all cases. The reason is that the interface thickness increases as the droplet evaporates more, which results in more diffusion and faster evaporation.

Figure 9(a) shows the results at different surrounding temperature when $h^{lv} = 0.1$. It can be seen that an increase of the ambient temperature is responsible for faster evaporation. In fact, more thermal energy is transferred to the droplet by the warmer surrounded air, which allows droplet molecules to escape more rapidly. A comparison between the time history of the numerical results and D^2 law with $T_r = 0.9$ and various latent heats are shown in Fig. 9(b). It is clear that by increasing

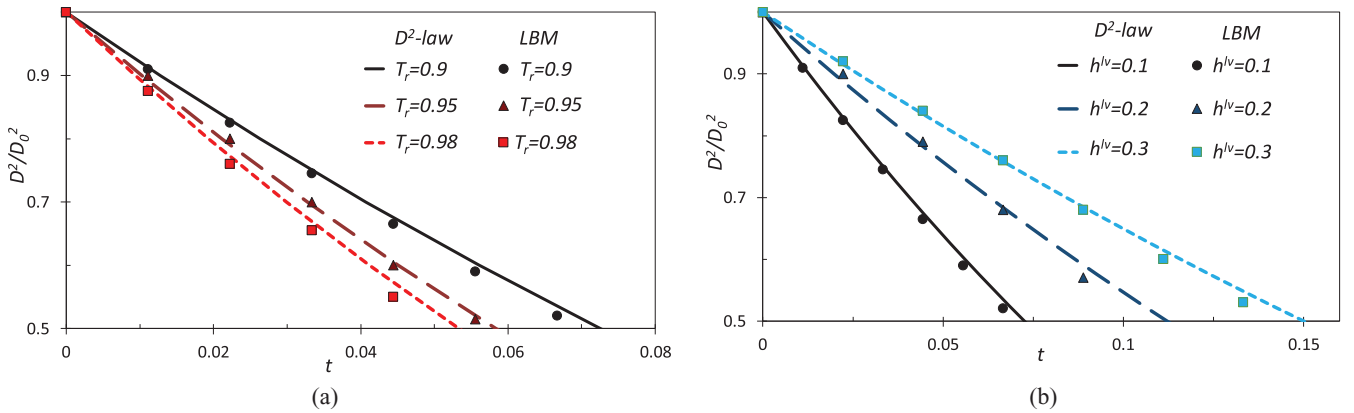

FIG. 9. Comparison between time histories of the numerical results and D^2 law for (a) different hot boundary temperature with $h^{lv} = 0.1$ and (b) different latent heat at $T_r = 0.9$.

the value of the latent heat, the speed of the evaporation decreases as more energy is required to transform a given quantity of liquid into vapor. Therefore we can conclude that the lifetime of an evaporating droplet depends on the manner in which it evaporates. It should be mentioned that the LBM results deviate from the D^2 law significantly as the size of the droplet becomes smaller than 0.4 in Fig. 9 due to the evaporation. Our numerical results deviate from the D^2 law for $D^2/D_0^2 < 0.4$.

C. Falling evaporating droplet

As the droplet falls, the gravity force initially causes the droplet to continuously speed up. However, by increasing the velocity the air drag force increases until, eventually, the air drag force is exactly equal to the force of gravity, and there is no net force acting on the droplet. When gravity and drag forces are exactly balanced, the droplet reaches a steady-state condition and will no longer speed up or slow down but will continue falling at a constant velocity, called the terminal velocity.

The hydrodynamics and shape deformation of a falling droplet are characterized by the Eötvös number (Eo, also called the Bond number), Reynolds number (Re), and the Weber number (We):

$$\mathrm{Eo} = \frac{g(\rho_{liq} - \rho_{vap})D_0^2}{\sigma}, \tag{25}$$

$$\mathrm{Re} = \frac{U_t D_0}{\nu_{vap}}, \tag{26}$$

$$\mathrm{We} = \frac{\rho_{vap} U_t^2 D_0}{\sigma}, \tag{27}$$

where g is the magnitude of the gravitational acceleration, U_t is the terminal velocity, and μ_{vap} is the dynamic viscosity of vapor. Generally, a higher Re number would induce larger deformation of the droplet due to the formation of the recirculation regions behind the droplet. The Eo number controls the deformability of the droplet away from a spherical shape. A higher Eo number allows larger deformation. The importance of surface tension is indicated by the We number. A droplet with larger We number (i.e., smaller surface tension) deforms more compared to a droplet with a smaller We number (or higher surface tension) [1]. Note that the Weber number is often replaced by either the Ohnesorge number ($\mathrm{Oh} = \sqrt{\mathrm{We}}/\mathrm{Re}$) or the Morton number ($\mathrm{Mo} = \mathrm{EoOh}^4$) which comprise physical properties and droplet diameter only.

Figure 10 shows the effect of various density ratios on the terminal velocity of a falling droplet with $D_{0,\mathrm{LB}} = 60$, and $\tau = 1$ and $g = 5 \times 10^{-7}$. It can be seen that increased density ratio leads to higher terminal velocity. As a result, the droplet will reach a larger distance in the same amount of time and it takes more time for the denser droplet to reaches its steady-state condition. For all cases, the final shape of the droplet is similar and spherical. Our results are consistent with the results presented by Hua and Luo [63] which indicated that the effect of the density ratio is more significant in terminal velocity than in the final shape. Since the droplet falling is driven by the gravity, the density ratio has a significant effect on the droplet motion and deformation. For the higher ρ^*, the Eo number is higher and the inertia and the driving force is larger than that for the lower ρ^*. By increasing the driving force, stronger recirculation regions behind the falling droplets are formed which lead to larger deformation for the higher density ratios [1]. The inertial effect on the droplet motion of high ρ^* is stronger and, consequently, its falling velocity is larger than the droplet with lower ρ^*.

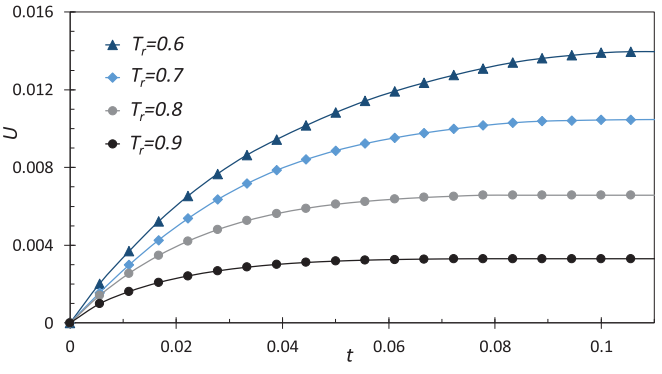

FIG. 10. Effect of density ratio on variation of velocity of a falling droplet. Here, $\rho^* = 6, 15, 40$, and 130 are equivalent with $T_r = 0.9, 0.8, 0.7$, and 0.6, respectively.

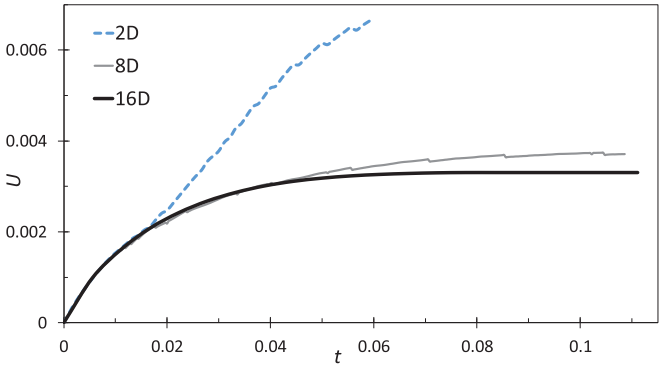

FIG. 11. Effect of streamwise length on terminal velocity of droplet with $\rho^* = 6$.

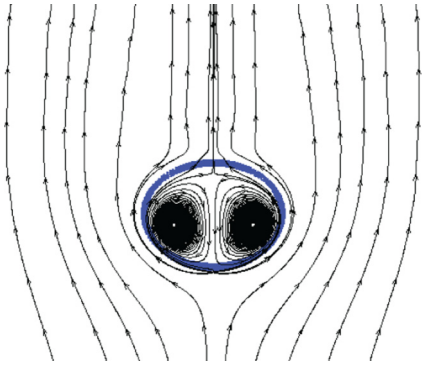

FIG. 13. Streamlines and inner circulation regions for the moving evaporating droplet at $t = 0.022$. (Note that the velocity vectors, as shown in Fig. 12, are plotted with respect to the fixed coordinate system (i.e., domain reference frame), whereas the true streamlines, as shown in this figure, are plotted by using the relative velocity with respect to the droplet. Here, the streamlines are calculated in the frame of reference fixed to the bottom of the droplet.

In this paper, all of the falling droplet simulations are done in a fully periodic domain of width $8D_0$ to prevent the boundaries' proximity effect on the results [64,65]. If the side boundaries are close to the droplet, it achieves its terminal state in a shorter distance with smaller terminal velocity and its final shape is also different from that in an infinite medium. Note that, if the droplet crosses the bottom or top boundaries, it may affect itself. Our analysis indicates that if we choose a short streamwise length when using a periodic boundary condition, the falling droplet affects itself when passing the boundaries and the fall velocity and shape of the drop may significantly change. The effect of short streamwise length on simulation results is stronger at smaller density ratios. In order to show the effect of boundaries on terminal velocity, falling of a droplet with $\rho^* = 6$ for different streamwise lengths is shown in Fig. 11. It can be seen that the droplet accelerates continuously during falling if we set a small streamwise length (i.e., $2D_0$). When the streamwise length is $8D_0$, a steady-state velocity is obtained. However, in this case the streamwisee length is not large enougth as some small jumps in the velocity are observed that are related to the times that the droplet crosses the boundaries during falling. By choosing the streamwise length equal to $16D_0$ a smooth profile for velocity is obtained. Therefore we recommend to choose a large enough (i.e., longitudinal size $> 16D_0$) domain to let the drop fall free from boundary effects.

Now, we study the the evaporation of a moving droplet falling under gravity. For this purpose, the initial diameter of the droplet in lattice units is set as $D_{0,\mathrm{LB}} = 60$ and after achieving the equilibrium condition at $T_r = 0.8$, the droplet starts to move due to the gravity ($g = 1.5 \times 10^{-5}$), and then after reaching its terminal velocity, the droplet is subjected to heat flux $\dot{Q} = 8.1 \times 10^{-7}$ and phase change enthalpy $h^{lv} = 0.1$. The computational domain is $10D_0 \times 20D_0$ and the constant pressure boundary condition is applied for the side boundaries and the periodic boundary condition is used for the upper and lower boundaries.

The time evolution of the density field and the shape of the drop are shown in Fig. 12. It can be seen that as time progresses [see Figs. 12(b)–12(d)], the shape of the droplet tends to become circular. The reason is that over time, the size of the droplet diminishes due to the evaporation. As we discussed before, smaller droplets tend to have a circular shape during the falling and the flow regime approaches to Stokes'

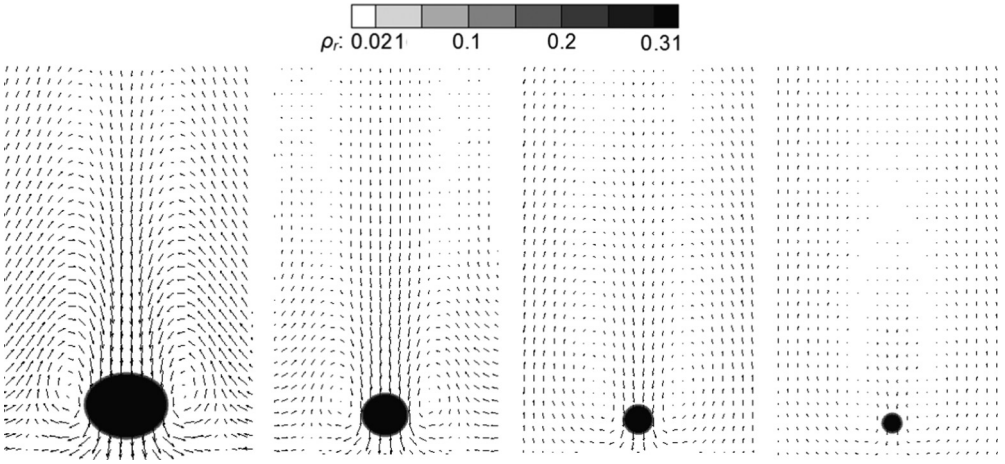

FIG. 12. The time evaluation of density and instantaneous velocity field for moving an evaporating droplet. From left to right: $t = 0$,$t = 0.039$,$t = 0.072$, and $t = 0.1$. (Note: At $t = 0$ the droplet is moving with its terminal velocity; i.e., $U_{t,\mathrm{LB}} = 0.06$ in lattice units).

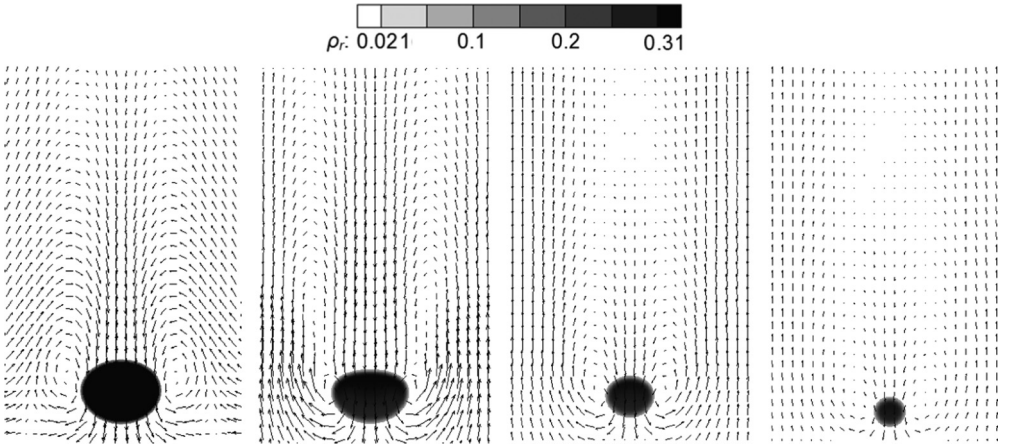

FIG. 14. The time evaluation of density and instantaneous velocity field for moving an evaporating droplet in a fully periodic domain. From left to right: $t = 0, t = 0.039, t = 0.072$, and $t = 0.1$.

flow. Roughly, the length of a computational domain is covered four times by the droplet before full evaporation.

In order to better understand the effect of moving on the evaporation, we run the above case study again but this time for the stationary droplet. For this case the computational domain size is $10D_0 \times 10D_0$ and the rest of the computational parameters are the same as those of the moving case. Our study shows that the total time taken for the droplet to evaporate is 0.17 and 0.12 for stationary and moving cases, respectively. In other words, the moving droplet evaporates faster in comparison with the stationary one. In fact for the case of the moving droplet, a relative motion exists between the droplet and surrounding vapor which has a significant effect on the heat transfer. It can be seen that from Fig. 12 that there are two large recirculation regions (or wakes) at the left and right sides of the droplet. The maximum value of velocity is near the interface which applies shear stress at the interface. As a result of this shear, the liquid within the droplet starts to circulate which results in heat transfer enhancement and increase in evaporation rate. Figure 13 shows the streamlines and internal circulations for the moving droplet at $t = 0.022$. The circulation structure is strongly related to the degree of deformation, the terminal velocity, and the size of the droplet. A general conclusion—in agreement with real-life physics—is that, due to the motion of the droplet, convective transport significantly increases the component transport across the interface as well as the supply of heat for the evaporation. However, over time the size of the droplet and, consequently, the size of the wakes become smaller and as a result, the effect of convection on the heat transfer enhancement becomes smaller, as for a very small droplet the effect is negligible.

In order to examine the effect of the boundary condition on the simulation results, we resimulate the test case of Fig. 11 in a fully periodic domain. The time evolution of the density field and the shape of the drop are shown in Fig. 14. It is clear that the droplet deforms more during evaporation compared to the nonevaporating case. As we discussed earlier, the density of the droplet decreases during the evaporation in a fully periodic domain. As a result, the droplet deforms more during the movement. However, the size of the droplet diminishes over time due to the evaporation and the shape of the droplet becomes circular. We found that the droplet in a

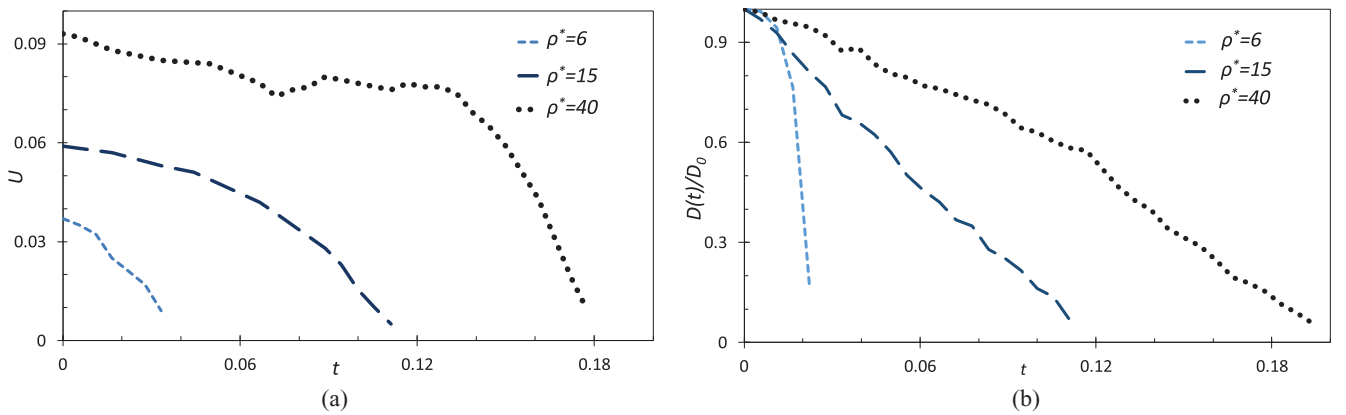

FIG. 15. (a) The instantaneous velocity and (b) the equivalent spherical diameter of an evaporating falling droplet with various density ratios.

fully periodic domain evaporates slightly faster (i.e., $\approx$ 5000 iterations) which is due to the density changes of the droplet during evaporation.

The instantaneous velocity and the normalized equivalent spherical diameter of the evaporating falling droplet with different density ratios are shown in Figs. 15(a) and 15(b), respectively. Evaporation is started at $t = 0$ when the droplet is moving with its terminal velocity. It can be seen from Fig. 15(a) that it take more time for a droplet with higher density ratio to evaporate completely. It can be seen that the droplet corresponding to $\rho^* = 40$ (and higher) exhibits a wobbling and oscillating motion due to the vortices that are shaped around the droplet. This wobbling results in variations in shape and velocity of the droplet during evaporation.

From Fig. 15(a) and also Fig. 10 we realize that the terminal velocity corresponding to $\rho^* = 40$ is close to 0.1, which is usually defined as a maximum threshold for velocity in the LBM to have small compressibility error as well as accurate results. By increasing the density ratio the value of the terminal velocity increases as it is around 0.19 for $\rho^* = 130$. Our analysis showed that the effects of compressibility error become significant. As we mentioned earlier, the falling droplet wobbles during evaporation at the high density ratio. The effect of wobbling as well as the effect of compressibility error result in unstable simulation for evaporating cases with $\rho^* > 50$. However, it is possible to improve the model to higher density ratios by tuning the computational parameters such as gravity or resolution. However, we will be restricted to small sizes (small Re or low density ratios) when using the presented PP-LBM due to some inherent limitations of the model as well as some computational considerations to have stable simulations.

V. CONCLUSION

The dynamics of a single droplet undergoing evaporation and downfall was simulated and studied by a single-component pseudopotential lattice Boltzmann model. Evaporation was driven by adding required source terms to the thermal equation. At first, the model was applied to model a stationary droplet with and without evaporation. We showed that the method is capable and accurate and our numerical results were in good agreement with theory. Finally, the method was expanded to study the dynamics of a falling evaporating droplet. The thermohydrodynamics of the fluid flow, as well as computational limitations, were discussed. The results showed that due to the movement of the droplet, a convection phenomenon occurs in the system which makes diffusion over the interface and significantly increases the rate of evaporation. However, the model is limited to low Re numbers for simulating a falling droplet undergoing a phase change.

ACKNOWLEDGMENTS

The research leading to these results has been done in cooperation with the Dutch Institute for Sustainable Process Technology (ISPT) and Shell Amsterdam as a part of the LBM project.

[1] M. J. Ni, S. Komori, and N. B. Morley, Int. J. Heat Mass Transfer. **49**, 366 (2006).
[2] E. Loth, Prog. Energy Combust. Sci. **26**, 161 (2000).
[3] S. S. Sazhin, Prog. Energy Combust. Sci. **32**, 162 (2006).
[4] H. S. Udaykumar, R. Mittal, and W. Shyy, J. Comput. Phys. **153**, 535 (1999).
[5] G. Tryggvason, B. Bunner, A. Esmaeeli, D. Juric, N. Al-Rawahi, W. Tauber, J. Han, S. Nas, and Y. J. Jan, J. Comput. Phys. **169**, 708 (2001).
[6] S. G. Yoon, Ph.D. thesis, Purdue University, 2002.
[7] B. J. Daly, Phys. Fluids **12**, 1340 (1969).
[8] C. W. Hirt and B. D. Nichols, J. Comput. Phys. **39**, 201 (1981).
[9] S. Tanguy, T. Menard, and A. Berlemont, J. Comput. Phys. **221**, 837 (2007).
[10] J. Bao and L. Schaefer, Appl. Math. Modell. **37**, 1860 (2013).
[11] L. Chen, Q. Kang, Y. Mua, Y. L. He, and W. Q. Tao, Int. J. Heat Mass Transfer **76**, 210 (2014).
[12] Q. Li, K. H. Luo, Q. J. Kang, Y. L. He, Q. Chen, and Q. Liu, Prog. Energy Combust. **52**, 62 (2016).
[13] A. K. Gunstensen, D. H. Rothman, S. Zaleski, and G. Zanetti, Phys. Rev. A **43**, 4320 (1991).
[14] H. Liu, A. J. Valocchi, and Q. Kang, Phys. Rev. E **85**, 046309 (2012).
[15] X. Shan and H. Chen, Phys. Rev. E **47**, 1815 (1993).
[16] M. R. Swift, W. R. Osborn, and J. M. Yeomans, Phys. Rev. Lett. **75**, 830 (1995).
[17] C. M. Pooley and K. Furtado, Phys. Rev. E **77**, 046702 (2008).
[18] X. He, S. Chen, and R. Zhang, J. Comput. Phys. **152**, 642 (1999).
[19] H. Liu, A. J. Valocchi, Y. Zhang, and Q. Kang, Phys. Rev. E **87**, 013010 (2013).
[20] A. Mazloomi M, S. S. Chikatamarla, and I. V. Karlin, Phys. Rev. Lett. **114**, 174502 (2015).
[21] Y. Gan, A. Xu, G. Zhang, and S. Succi, Soft Matter **11**, 5336 (2015).
[22] Q. Li and K. H. Luo, Appl. Therm. Eng. **72**, 56 (2014).
[23] M. Sbragaglia, R. Benzi, L. Biferale, S. Succi, K. Sugiyama, and F. Toschi, Phys. Rev. E **75**, 026702 (2007).
[24] S. Khajepor, J. Wen, and B. Chen, Phys. Rev. E **91**, 023301 (2015).
[25] P. Yuan and L. Schaefer, Phys. Fluids **18**, 042101 (2006).
[26] A. L. Kupershtokh, D. A. Medvedev, and D. I. Karpov, Comput. Math. Appl. **58**, 965 (2009).
[27] A. Zarghami, N. Looije, and H. Van den Akker, Phys. Rev. E **92**, 023307 (2015).
[28] G. R. McNamara, A. L. Garca, and B. J. Alder, J. Stat. Phys. **97**, 1111 (1997).
[29] Y. Shi, T. S. Zhao, and Z. L. Guo, Phys. Rev. E **70**, 066310 (2004).
[30] A. Zarghami, S. Ubertini, and S. Succi, Comput. Fluids **77**, 56 (2013).
[31] J. Ghasemi and S. E. Razavi, Comput. Math. Appl. **60**, 1135 (2010).
[32] V. Sofonea, A. Lamura, G. Gonnella, and A. Cristea, Phys. Rev. E **70**, 046702 (2004).

[33] G. Gonnella, A. Lamura, and V. Sofonea, Phys. Rev. E **76**, 036703 (2007).
[34] A. Cristea, G. Gonnella, A. Lamura, and V. Sofonea, Math. Comput. Simul. **72**, 113 (2006).
[35] P. Lallemand and L.S. Luo, Int. J. Mod. Phys. B **17**, 41 (2003).
[36] G. Gonnella, A. Lamura, and V. Sofonea, Eur. Phys. J. Spec. Top. **171**, 181 (2009).
[37] X. He, S. Chen, and G. D. Doolen, J. Comput. Phys. **146**, 282 (1998).
[38] Z. Guo, C. Zheng, B. Shi, and T. S. Zhao, Phys. Rev. E **75**, 036704 (2007).
[39] A. D'Orazio and S. Succi, Future Gener. Comput. Syst. **20**, 935 (2004).
[40] A. Zarghami, S. Di Francesco, and C. Biscarini, Int. J. Mod. Phys. C **25**, 1350086, (2014).
[41] H. N. Dixit and V. Babu, Int. J. Heat Mass Transfer **49**, 727 (2006).
[42] L. S. Luo, Phys. Rev. Lett. **81**, 1618 (1998).
[43] H. Huang, M. Krafczyk, and X. Lu, Phys. Rev. E **84**, 046710 (2011).
[44] Q. Li, K. H. Luo, and X. J. Li, Phys. Rev. E **86**, 016709 (2012).
[45] S. Gong and P. Cheng, Int. J. Heat Mass Transfer **55**, 4923 (2012).
[46] S. Gong and P. Cheng, Comput. Fluids **53**, 93 (2012).
[47] K. Sankaranarayanan, X. Shan, I. G. Kevrekidis, and S. Sundaresan, J. Fluid Mechanics **452**, 61 (2002).
[48] Y. Peng, C. Shu, and Y. T. Chew, Phys. Rev. E **68**, 026701 (2003).
[49] A. Zarghami, S. Ubertini, and S. Succi, Int. J. Numer. Methods Heat Fluid Flow **24**, 270 (2014).
[50] Q. Li and K. H. Luo, Phys. Rev. E **89**, 053022 (2014).
[51] W. Deen, *Analysis of Transport Phenomena* (Oxford University Press, Oxford, 1998).
[52] A. Markus and G. Hazi, Phys. Rev. E **83**, 046705 (2011).
[53] M. R. Kamali, J. J. J. Gillissen, H. E. A. van den Akker, and S. Sundaresan, Phys. Rev. E **88**, 033302 (2013).
[54] H. Ding and C. J. Yuan, J. Comput. Phys. **273**, 243 (2014).
[55] Y. Wang, C. Shu, and L.M. Yang, J. Comput. Phys. **302**, 41 (2015).
[56] S. Mukherjee, A. Zarghami, C. Haringa, S. Kenjereš, and H. E. A. Van den Akker, A comparative assessment of lattice Boltzmann and volume of fluid (VOF) approaches for generic multiphase problems, in *Proceedings of the 9th International Conference on Multiphase Flow*, May 22–27,2016, Firenze, Italy.
[57] L. Zheng, T. Lee, Z. Guo, and D. Rumschitzki, Phys. Rev. E **89**, 033302 (2014).
[58] H. Safari, M. H. Rahimian, and M. Krafczyk, Phys. Rev. E **90**, 033305 (2014).
[59] D. Albernaz, M. Do-Quang, and G. Amberg, Phys. Rev. E **91**, 043012 (2015).
[60] A. J. Wagner, Phys. Rev. E **74**, 056703 (2006).
[61] E. S. Kikkinides, A. G. Yiotis, M. E. Kainourgiakis, and A. K. Stubos, Phys. Rev. E **78**, 036702 (2008).
[62] M. Sbragaglia and D. Belardinelli, Phys. Rev. E **88**, 013306 (2013).
[63] G. A. E. Godsave, Symp. (Int.) Combust., [Proc.] **4**, 818 (1953).
[64] J. Hua and J. Lou, J. Comput. Phys. **222**, 769 (2007).
[65] K. Mukundakrishnan, S. Quan, D. M. Eckmann, and P. S. Ayyaswamy, Phys. Rev. E **76**, 036308 (2007).